Shape sensitivity of thermoacoustic oscillations in an annular combustor with a 3D adjoint Helmholtz solver

Ekrem Ekici[a], Stefano Falco[a], Matthew P. Juniper[a,*]

[a]*Engineering Department, Trumpington Street, Cambridge, CB2 1PZ, United Kingdom*

Abstract

We model acoustic oscillations driven by velocity-coupled heat release rate fluctuations. We obtain an inhomogenous wave equation and convert it to the frequency domain with a modal decomposition. We impose acoustic boundary conditions and, using a finite element discretization with Lagrange elements, express this as a nonlinear eigenvalue problem for the complex angular frequency, ω. We solve this using the open source platform FEniCS combined with the SLEPc, PETSc and OpenMPI libraries. In Hadamard form we write the derivative of the eigenvalue, ω, with respect to generic geometry changes. This requires the solution of the adjoint equation, which we obtain with the same method as the direct equation. The output is a thermoacoustic Helmholtz solver that cheaply calculates the effect of generic shape changes on the growth rate and frequency of thermoacoustic oscillations. We then consider symmetry-preserving and symmetry-breaking geometry modifications. For demonstration we model a 30kW laboratory-scale annular combustor (MICCA from EM2C). We parametrize the surfaces of the three-dimensional geometry with NURBS using control points. For the plenum and the combustion chamber, we find the eigenvalue shape derivatives with respect to the parameters of these control points. We apply two different strategies, perpendicular boundary movements and control point perturbations, to implement shape changes proportional to these shape derivatives, thereby reducing the growth rate of the unstable mode

*Corresponding author
Email address: mpj1001@cam.ac.uk (Matthew P. Juniper)

by increasing the phase shift between the pressure and the heat release rate oscillations. This computational method shows how to significantly alter thermoacoustic oscillations by making small geometry changes. The framework in this paper can handle arbitrarily complex three-dimensional geometries, which will be useful for the design of industrial combustion systems.
Keywords: thermoacoustic instability, adjoint method, Helmholtz solver, sensitivity analysis, shape optimization

1. Introduction

Thermoacoustic instabilities are a major threat to the safe operation of gas turbines and rocket engines. During the combustion process, chemical energy is converted into thermal energy. The fluctuations in the heat release rate excite acoustic waves that in turn interact with the flame. If the pressure and heat release rate oscillations are sufficiently in phase, then the acoustic energy grows, until balanced by the energy loss due to damping or acoustic radiation from the boundaries [1, 2]. These oscillations can become large enough to cause noise, vibrations or, in the worst cases, extinction of the flame or structural damage. Thermoacoustic systems are sensitive to small changes to their design and operating parameters [3]. They can appear in the late stages of the design process [4], requiring costly re-design. This motivates the development of tools that could accurately and cheaply identify the design changes that most stabilize a thermoacoustic system.

Various modelling approaches can be used during the design process, such as acoustic network models [5], Helmholtz solvers [6, 7, 8] and large eddy simulations [9] of the flame or entire combustion systems [10]. This paper focuses on Helmholtz solvers because they provide more geometric flexibility than network models but are computationally much cheaper than LES. We use adjoint methods to compute the sensitivity of the thermoacoustic growth rate and frequency to geometry modifications. Adjoint-based sensitivity analysis was applied to a simple thermoacoustic system by [11]. They computed feedback and

base state sensitivities of the eigenvalues of a Rijke tube with a hot wire, modelled as a time-delay system, which was later confirmed experimentally by [12]. Adjoint-based sensitivity analysis and gradient-based optimization were applied to network models of a longitudinal [13] and an annular combustor [14], which led to stabilization of all the modes by changing the network geometry. In the network model in those studies, the geometry changes were limited to radii and length changes. In a Helmholtz solver, however, geometry changes can be three-dimensional and non-uniform. In Helmholtz solvers, adjoint equations have been used for uncertainty quantification in a longitudinal combustor [15] and for the optimal placement and tuning of acoustic dampers in an annular combustor [16]. The effect of high-order perturbations for symmetry-breaking changes to the three-dimensional combustor is investigated in [17] via an adjoint Helmholtz solver. The azimuthal mode degeneracy is lost due to asymmetric changes in the FTF. The shape sensitivity of a Rijke tube using a parameter-free approach and a 3D Helmholtz solver was performed in [18]. That approach is easier to implement than writing the shape sensitivity in Hadamard form but is more computationally expensive because it requires the calculation of shape gradients for each mesh node. Similarly, shape optimization of a Rijke tube and a turbulent swirl combustor using parametric shapes and a 2D Helmholtz solver was carried out in [19]. By applying small geometry modifications, they managed to stabilize both systems. The theory, numerical methods, and technical challenges of developing adjoint thermoacoustic Helmholtz solvers were outlined in [20] for 1D solvers and a review of the use of adjoints in thermoacoustics can be found in [21].

Parametrization of complex shapes poses a significant technical challenge in shape optimization. The NURBS representation used here facilitates the design process because it allows the manipulation of the entire geometry thorough a small number of control points [22]. The gradient of the cost function with respect to the parameters of the NURBS control points can be found cheaply with adjoint methods. As the geometric complexity increases, the number of parameters increases, but the computational expense of the adjoint calculation

does not increase because the gradient with respect to all parameters is found with a single calculation. This procedure has been applied to wing shape and turbine blade geometry optimization [23, 24].

In this article, we show how to reduce the growth rate of unstable azimuthal and mixed modes of a laboratory-scale annular combustor (MICCA) by modifying the geometry using NURBS control points. In Section 2 we describe the theoretical and numerical aspects of the Helmholtz solver. In Section 3 we derive the formulae of the eigenvalue shape derivative (in Hadamard form) for different boundary conditions in the case of simple and semi-simple degenerate eigenvalues. In Section 4 we describe the discrete model of the MICCA combustor. In Section 5 we explain a detailed shape sensitivity analysis considering symmetry-preserving and symmetry breaking geometry modifications. In Section 6 we apply symmetry-preserving modifications to the shape of the combustor, reducing the growth rate of the unstable azimuthal and mixed mode by modifying the plenum and the combustion chamber applying perpendicular boundary or control point perturbations. After the iteration, we reveal the physical mechanism behind the growth rate's reduction. Finally, in Section 7 we apply the same procedure as in Section 6 with symmetry-breaking geometry modifications.

2. Thermoacoustic Helmholtz solver

In this section we review the modelling and the numerical analysis of the Helmholtz solver [6, 20]. We start by considering a compressible, reacting, inviscid flow. The fluid is modelled as a perfect gas. We want to study the evolution of small perturbations superimposed onto a zero Mach number mean flow. The bar, $\bar{(\cdot)}$, will denote a steady mean quantity and the prime, $(\cdot)'$, an unsteady perturbation quantity. We write the linearized momentum and energy equations

$$\frac{\partial \boldsymbol{u}'}{\partial t} + \frac{1}{\bar{\rho}} \boldsymbol{\nabla} p' = 0 \tag{1a}$$

$$\frac{\partial p'}{\partial t} + \gamma \bar{p} \boldsymbol{\nabla} \cdot \boldsymbol{u}' = (\gamma - 1)\dot{q}' \tag{1b}$$

where $\boldsymbol{u}'$ is the velocity perturbation, p' is the pressure perturbation, $\dot{q}'$ is the heat release rate perturbation per unit volume, $\bar{\rho}$ is the mean density, $\bar{p}$ is the mean pressure, which is constant, and γ is the heat capacity ratio. If we take $\gamma \bar{p} \boldsymbol{\nabla} \cdot (1\text{a}) - \frac{\partial}{\partial t}(1\text{b})$, we obtain an inhomogeneous wave equation for the pressure perturbation.

$$\boldsymbol{\nabla} \cdot \left(\bar{c}^2 \boldsymbol{\nabla} p' \right) - \frac{\partial^2 p'}{\partial t^2} = -(\gamma - 1) \frac{\partial \dot{q}'}{\partial t} \tag{2}$$

where $\bar{c} = \sqrt{\gamma \bar{p} / \bar{\rho}}$ is the mean speed of sound. We use the method of separation of variables

$$(\cdot)'(\boldsymbol{x}, t) = \mathrm{Re}\Big\{ \hat{(\cdot)}(\boldsymbol{x}) e^{-i\omega t} \Big\} \tag{3}$$

to obtain an inhomogeneous Helmholtz equation.

$$\boldsymbol{\nabla} \cdot \left(\bar{c}^2 \boldsymbol{\nabla} \hat{p} \right) + \omega^2 \hat{p} = i\omega(\gamma - 1)\hat{q} \tag{4}$$

where ω is the complex eigenvalue, of which the real part is the angular frequency and the imaginary part is the growth rate. In this formulation, an eigenvalue is linearly unstable if its growth rate, ω_i, is positive.

The unsteady heat release rate is modelled in terms of the linear response of the flame to small velocity perturbations. In this paper we assume that the local heat release rate perturbation, $\hat{q}$, is uniform across the flame volume and is zero elsewhere, although this assumption is easily relaxed:

$$\frac{\hat{\dot{q}}}{\bar{\dot{q}}} = F(\omega) \frac{\hat{\boldsymbol{u}}(\boldsymbol{x}_r) \cdot \boldsymbol{n}_r}{\bar{u}} \tag{5}$$

where $\bar{\dot{q}} = \bar{\dot{Q}} / V_f$ is the thermal power of the flame per unit volume (where $\bar{\dot{Q}}$ is the total thermal power of the flame and V_f is the flame volume), $F(\omega)$ is the flame transfer function (FTF), $\hat{\boldsymbol{u}}(\boldsymbol{x}_r) \cdot \boldsymbol{n}_r$ is the component of the velocity perturbation along the unit vector $\boldsymbol{n}_r$, evaluated at the reference point $\boldsymbol{x}_r$, and $\bar{u}$ is the average flow velocity at the reference point.

By combining Eq. (1a), written in the frequency domain, and Eq. (5), we can express the flame response as a function of the pressure gradient. We

substitute the resulting expression into (4) to obtain:

$$\boldsymbol{\nabla} \cdot \left(\bar{c}^2 \boldsymbol{\nabla} \hat{p}\right) + \omega^2 \hat{p} = \frac{\bar{\dot{q}}}{\bar{u}} \frac{\gamma - 1}{\bar{\rho}(\boldsymbol{x}_r)} F(\omega) \boldsymbol{\nabla} \hat{p}(\boldsymbol{x}_r) \cdot \boldsymbol{n}_r \tag{6}$$

Annular combustors consist of a number of annular sectors. When the interaction between neighbouring flames is negligible, we can assume that the sectors are independent, meaning that the mass flow rate fluctuations in one injector influence the fluctuating heat release rate in that sector but not in the other sectors [25]. We also assume that the flame transfer function is the same for each sector.

In general, we impose Robin boundary conditions for the acoustics.

$$\boldsymbol{\nabla} \hat{p} \cdot \boldsymbol{n} - \frac{i\omega}{\bar{c}Z} \hat{p} = 0 \tag{7}$$

where $\boldsymbol{n}$ is the outward unit normal and Z is the specific acoustic impedance [26], defined as the non-dimensional ratio of the acoustic pressure to the normal component of the acoustic velocity

$$Z = \frac{\hat{p}}{\bar{\rho}\bar{c}\hat{\boldsymbol{u}} \cdot \boldsymbol{n}} \tag{8}$$

For one special case, $Z \to 0$ at an ideal open boundary, i.e. the acoustic pressure tends to zero and we obtain Dirichlet (sound-soft) boundary conditions, $\hat{p} = 0$. For another special case, $Z \to \infty$ at an ideal closed boundary, i.e. the acoustic velocity tends to zero and we obtain Neumann (sound-hard) boundary conditions, $\boldsymbol{\nabla} \hat{p} \cdot \boldsymbol{n} = 0$.

Equations (6) and (7) are discretized using the Bubnov-Galerkin finite element method, in which the trial and test functions belong to the same function space. We use P1 and P2 elements. The finite element approximation results in a nonlinear eigenvalue problem for the complex angular frequency ω.

$$\mathbf{A}\mathbf{p} + \omega \mathbf{B}\mathbf{p} + \omega^2 \mathbf{C}\mathbf{p} - \mathbf{D}(\omega)\mathbf{p} = 0 \tag{9}$$

where $\mathbf{A}$ is the mass matrix and $\mathbf{C}$ is the stiffness matrix. The unsteady heat release matrix $\mathbf{D}(\omega)$ depends nonlinearly on the eigenvalue ω. $\mathbf{B}$ contains the Robin boundary conditions. In this paper these boundary conditions are not

frequency-dependent, although it is easy to make them frequency-dependent by treating $\mathbf{B}$ in the same way as $\mathbf{D}$. The problem is nonlinear in the eigenvalue and linear in the eigenvector.

The nonlinear eigenvalue problem (9) is solved using fixed-point iteration with relaxation [7]. After finding the solution, we normalize the eigenvector, $\hat{p}$, such that $\langle \hat{p} | \hat{p} \rangle = 1$. The code is written with the open source computing platform FEniCS [27, 28]. The weak forms in Eq. (6) are defined using the UFL package [29]. At each iteration k, the generalized eigenvalue problem, $(\mathbf{A} + \omega_k \mathbf{B} - \mathbf{D}(\omega_k))\mathbf{p} + (\omega_k^2)\mathbf{C}\mathbf{p} = 0$, is solved with the EPS solver in the SLEPc library [30]. All the matrices are assembled within the subroutines of DOLFINx apart from the active flame matrix ($\mathbf{D}$). This matrix is generated explicitly using the PETSc package [31]. A shift-and-invert spectral transformation is used to enhance the convergence of eigenvalues in the neighbourhood of a given value. The solver is parallelized with the OpenMPI library [32].

3. Shape derivatives

We wish to calculate how small modifications to the geometry of a combustor affect the stability of the thermoacoustic modes. This translates into the problem of finding the derivative of an eigenvalue with respect to arbitrary perturbations to the shape of the domain [33].

3.1. Shape derivative and Hadamard theorem

Hadamard's structure theorem [34] shows how to calculate general shape derivatives from a single deformation field. This provides a computationally-cheap method to calculate shape derivatives. Following [35], we define a one-parameter family of linear mappings.

$$T_t(\boldsymbol{x}) = \boldsymbol{x} + t\boldsymbol{V}(\boldsymbol{x}) \tag{10}$$

where t is the parameter of the transformation and $\boldsymbol{V}$ is a continuous vector field, representing the direction of the shape perturbation. T_t transforms the

domain Ω into the deformed domain Ω_t.

$$\Omega_t = T_t(\Omega) \tag{11}$$

Let $\mathcal{J}$ be a shape functional, which is a functional that depends on the shape of the domain.

The shape derivative of $\mathcal{J}$ at Ω in the direction $\boldsymbol{V}$ is defined through the Gateaux derivative [36], where the square brackets indicate that $[\boldsymbol{V}]$ is a vector in the direction of the shape gradient to be calculated:

$$\mathrm{d}\mathcal{J}(\Omega)[\boldsymbol{V}] = \lim_{t \to 0^+} \frac{\mathcal{J}(\Omega_t) - \mathcal{J}(\Omega)}{t} \tag{12}$$

A shape functional $\mathcal{J}$ is shape differentiable at Ω if the derivative exists for all the directions $\boldsymbol{V}$ and if the mapping $\boldsymbol{V} \mapsto \mathrm{d}\mathcal{J}(\Omega)[\boldsymbol{V}]$ is linear and continuous.

As a mild smoothness assumption, we assume that the shape derivative $\mathrm{d}\mathcal{J}$ does not exist for every direction of the vector field $\boldsymbol{V}$, but only depends on the outward normal component of $\boldsymbol{V}$ at the boundary of the domain.

$$\mathrm{d}\mathcal{J}(\Omega)[\boldsymbol{V}] = \int_\Gamma C\, G \,\mathrm{d}S \tag{13}$$

where Γ is the domain boundary, $C = \boldsymbol{V} \cdot \boldsymbol{n}$, and G is the shape gradient. This result is known as the Hadamard theorem (or formula) [37, 38]. The shape derivative is said to be written in Hadamard form.

3.2. Shape derivatives under a state constraint

We want to derive a formula for the shape derivative in Hadamard form, or equivalently for the shape gradient of ω, where ω is an eigenvalue of the inhomogeneous Helmholtz equation. We consider Robin boundary conditions, which contain Dirichlet and Neumann boundary conditions as special cases. The boundary Γ is split into a non-deformable and a deformable part. The first is denoted by Γ_0 and the second by Γ_1. The problem reads

$$\mathcal{L}(\omega)\hat{p} = 0 \quad \text{in } \Omega \tag{14a}$$

$$\frac{\partial \hat{p}}{\partial n} - \frac{i\omega}{\bar{c}Z}\hat{p} = 0 \quad \text{on } \Gamma = \Gamma_0 \cup \Gamma_1 \tag{14b}$$

where $\mathcal{L}$ is the linear operator (acting linearly on the eigenfunction $\hat{p}$) of the inhomogeneous Helmholtz equation. We apply the perturbation T_t. Instead of solving the problem on the perturbed domain Ω_t, we map the perturbed problem onto the unperturbed domain Ω.

Let $\hat{p}_t$ solve (14) in the perturbed domain $\Omega_t = T_t(\Omega)$ and let $\boldsymbol{x}_t = T_t(\boldsymbol{x})$ be a point on the perturbed boundary. The material shape derivative is

$$\mathrm{d}\hat{p}[\boldsymbol{V}](\boldsymbol{x}) = \left.\frac{\mathrm{d}}{\mathrm{d}t}\right|_{t=0} \hat{p}_t(\boldsymbol{x}_t) \tag{15}$$

The local shape derivative is

$$\hat{p}'[\boldsymbol{V}](\boldsymbol{x}) = \left.\frac{\mathrm{d}}{\mathrm{d}t}\right|_{t=0} \hat{p}_t(\boldsymbol{x}) \tag{16}$$

The relation between the first, which is a total derivative, and the second, which is a partial derivative, is given by the chain rule

$$\mathrm{d}\hat{p}[\boldsymbol{V}] = \hat{p}'[\boldsymbol{V}] + \boldsymbol{\nabla}\hat{p} \cdot \boldsymbol{V} \tag{17}$$

The material derivative of any boundary condition is identically zero. In the case of a non-deformable boundary, $\boldsymbol{V} = 0$, and the material derivative is the local derivative. In the case of a deformable boundary, $\boldsymbol{V} \neq 0$. Using the chain rule (17), the shape derivative of the Dirichlet and Neumann boundary conditions are [39]

$$\hat{p}' = -C\frac{\partial \hat{p}}{\partial n} \tag{18}$$

$$\frac{\partial \hat{p}'}{\partial n} = -C\frac{\partial^2 \hat{p}}{\partial n^2} + \boldsymbol{\nabla}_\Gamma C \cdot \boldsymbol{\nabla}\hat{p} \tag{19}$$

We linearize (14). The material derivative of the Robin boundary condition is obtained by combining (18) with (19).

$$\mathcal{L}'(\omega)\omega'\hat{p} + \mathcal{L}(\omega)\hat{p}' = 0 \quad \text{in } \Omega \tag{20a}$$

$$\frac{\partial \hat{p}'}{\partial n} - \frac{i\omega}{\bar{c}Z}\hat{p}' = \frac{i\omega'}{\bar{c}Z}\hat{p} \quad \text{on } \Gamma_0 \tag{20b}$$

$$\frac{\partial \hat{p}'}{\partial n} - \frac{i\omega}{\bar{c}Z}\hat{p}' = -C\frac{\partial^2 \hat{p}}{\partial n^2} + \boldsymbol{\nabla}_\Gamma C \cdot \boldsymbol{\nabla}\hat{p} + \frac{i\omega}{\bar{c}Z}C\frac{\partial \hat{p}}{\partial n} + \frac{i\omega'}{\bar{c}Z}\hat{p} \quad \text{on } \Gamma_1 \tag{20c}$$

Given two square-integrable functions, f and g, we define the inner product $\langle f|g\rangle = \int_\Omega f^* g \,\mathrm{d}V$. Further, for an operator $\mathcal{L}$, we define its adjoint operator $\mathcal{L}^\dagger$ through the property $\langle \hat{p}^\dagger, \mathcal{L}\hat{p}\rangle = \langle \mathcal{L}^\dagger \hat{p}^\dagger, \hat{p}\rangle$. We multiply (20a) by $\hat{p}^{\dagger^*}$, which is the complex conjugate of the adjoint pressure, and integrate over the domain. Then we integrate the Laplace operator $\boldsymbol{\nabla}\cdot\bar{c}^2\boldsymbol{\nabla}(\cdot)$ by parts.

$$\left\langle \hat{p}^\dagger \middle| \mathcal{L}'(\omega)\hat{p}\right\rangle \omega' + \left\langle \mathcal{L}^\dagger(\omega^*)\hat{p}^\dagger \middle| \hat{p}'\right\rangle + \int_\Gamma \hat{p}^{\dagger^*}\bar{c}^2\frac{\partial \hat{p}'}{\partial n}\,\mathrm{d}S - \int_\Gamma \frac{\partial \hat{p}^{\dagger^*}}{\partial n}\bar{c}^2\hat{p}'\,\mathrm{d}S = 0 \tag{21}$$

The second term contains the adjoint equation. We substitute (20b) and (20c) into (21). We choose the adjoint boundary conditions in such a way as to eliminate the terms containing the term $\hat{p}'$ in (21).

$$\mathcal{L}^\dagger(\omega^*)\hat{p}^\dagger = 0 \quad \text{in } \Omega \tag{22a}$$

$$\frac{\partial \hat{p}^\dagger}{\partial n} + \frac{i\omega^*}{\bar{c}Z^*}\hat{p}^\dagger = 0 \quad \text{on } \Gamma \tag{22b}$$

The eigenvalues of the adjoint operator $\mathcal{L}^\dagger$ are the complex conjugates of the eigenvalues of $\mathcal{L}$. In the Bubnov-Galerkin finite element method there is no difference between the discrete adjoint and the discretization of the continuous adjoint because the resulting matrices for the weak formulations are identical[18]. Equation (21) becomes

$$\left(\left\langle \hat{p}^\dagger \middle| \mathcal{L}'(\omega)\hat{p}\right\rangle + \int_\Gamma \hat{p}^{\dagger^*}\frac{i\bar{c}}{Z}\hat{p}\,\mathrm{d}S\right)\omega' + \int_{\Gamma_1} \hat{p}^{\dagger^*}\bar{c}^2\left(-C\frac{\partial^2 \hat{p}}{\partial n^2} + \boldsymbol{\nabla}_\Gamma C\cdot\boldsymbol{\nabla}\hat{p} + \frac{i\omega}{\bar{c}Z}C\frac{\partial \hat{p}}{\partial n}\right)\mathrm{d}S = 0 \tag{23}$$

We can write a normalization condition for the adjoint pressure.

$$\left\langle \hat{p}^\dagger \middle| \mathcal{L}'(\omega)\hat{p}\right\rangle + \int_\Gamma \hat{p}^{\dagger^*}\frac{i\bar{c}}{Z}\hat{p}\,\mathrm{d}S = 1 \tag{24}$$

We use the adjoint boundary condition (22b) to eliminate the eigenvalue ω from the last term.

$$\omega' = \int_{\Gamma_1}\left(C\hat{p}^{\dagger^*}\bar{c}^2\frac{\partial^2 \hat{p}}{\partial n^2} - \boldsymbol{\nabla}_\Gamma C\cdot\left(\hat{p}^{\dagger^*}\bar{c}^2\boldsymbol{\nabla}\hat{p}\right) - C\frac{\partial \hat{p}^{\dagger^*}}{\partial n}\bar{c}^2\frac{\partial \hat{p}}{\partial n}\right)\mathrm{d}S \tag{25}$$

The eigenvalue sensitivity (or shape derivative) is written as a functional of $\hat{p}$ and $\hat{p}^\dagger$. The second term under the integral sign is, however, not yet in Hadamard form. We apply the tangential Stokes formula (A.3) with $f = C$ and $\boldsymbol{v} = \hat{p}^{\dagger^*}\bar{c}^2\boldsymbol{\nabla}\hat{p}$. We obtain the shape derivative for the Robin boundary conditions in Hadamard form.

$$\omega' = \int_{\Gamma_1} C\left(\hat{p}^{\dagger^*}\bar{c}^2\frac{\partial^2\hat{p}}{\partial n^2} - \kappa\hat{p}^{\dagger^*}\bar{c}^2\frac{\partial\hat{p}}{\partial n} + \operatorname{div}_\Gamma\left(\hat{p}^{\dagger^*}\bar{c}^2\boldsymbol{\nabla}\hat{p}\right) - \frac{\partial\hat{p}^{\dagger^*}}{\partial n}\bar{c}^2\frac{\partial\hat{p}}{\partial n}\right)\mathrm{d}S \quad (26)$$

where κ is the curvature. The shape derivative for the Dirichlet and the Neumann boundary conditions are special cases of Equation (26).

When applying Dirichlet boundary conditions, $\hat{p} = 0$, $\hat{p}^\dagger = 0$, $\boldsymbol{\nabla}\hat{p}^\dagger = \partial\hat{p}^\dagger/\partial n$ and $\boldsymbol{\nabla}\hat{p} = \partial\hat{p}/\partial n$, we obtain

$$\omega' = -\int_{\Gamma_1} C\left(\bar{c}^2\frac{\partial\hat{p}^{\dagger^*}}{\partial n}\frac{\partial\hat{p}}{\partial n}\right)\mathrm{d}S \quad (27)$$

When applying Neumann boundary conditions, $\partial\hat{p}/\partial n = 0$ and $\partial\hat{p}^\dagger/\partial n = 0$, we obtain

$$\omega' = \int_{\Gamma_1} C\left(\boldsymbol{\nabla}\cdot\left(\hat{p}^{\dagger^*}\bar{c}^2\boldsymbol{\nabla}\hat{p}\right)\right)\mathrm{d}S \quad (28)$$

If $\hat{q} = 0$ on the boundary, we obtain from (4)

$$\omega' = \int_{\Gamma_1} C\left(\bar{c}^2\boldsymbol{\nabla}\hat{p}^{\dagger^*}\cdot\boldsymbol{\nabla}\hat{p} - \omega^2\hat{p}^{\dagger^*}\hat{p}\right)\mathrm{d}S \quad (29)$$

3.3. The 2-fold degenerate case

To illustrate the semi-simple degenerate case, we write the formula for the eigenvalue shape derivative in Hadamard form

$$\int_{\Gamma_1} C\,G(\hat{p}^\dagger,\hat{p})\,\mathrm{d}S - \omega'\left\langle\hat{p}^\dagger\middle|\mathcal{L}'(\omega)\hat{p}\right\rangle = 0 \quad (30)$$

For repeated eigenvalues, two-fold degenerate in this case, the eigenfunction $\hat{p}$ is given by the linear combination

$$\hat{p} = \alpha_1\hat{p}_1 + \alpha_2\hat{p}_2 = \sum_{j=1}^{2}\alpha_j\hat{p}_j \quad (31)$$

where $\hat{p}_1$ and $\hat{p}_2$ are the independent eigenfunctions associated with the repeated eigenvalue ω and α_1 and α_2 are complex numbers. The same applies to the adjoint eigenfunction $\hat{p}^\dagger$. We substitute the linear combinations into (30)

$$\alpha_i^* \left(\int_{\Gamma_1} C\, G(\hat{p}_i^\dagger, \hat{p}_j)\, \mathrm{d}S - \omega' \left\langle \hat{p}_i^\dagger \middle| \mathcal{L}'(\omega) \hat{p}_j \right\rangle \right) \alpha_j = 0 \tag{32}$$

The shape gradient has now four components. We can normalize the bases of the two eigenspaces (direct and adjoint) such that they become biorthonormal

$$\left\langle \hat{p}_i^\dagger \middle| \mathcal{L}'(\omega) \hat{p}_j \right\rangle = \delta_{ij} \tag{33}$$

We are left with a 2×2 eigenvalue problem for the shape derivative ω'

$$\left(\int_{\Gamma_1} C\, G(\hat{p}_i^\dagger, \hat{p}_j)\, \mathrm{d}S - \omega' \delta_{ij} \right) \alpha_j = 0 \tag{34}$$

4. The MICCA combustor

The MICCA combustor is a laboratory-scale annular combustor at Laboratoire EM2C (CentraleSupélec) in France. Stable thermoacoustic limit cycles of standing and spinning azimuthal modes and a slanted mode are observed at some operating conditions [40, 41, 42].

4.1. Geometry

The MICCA combustor consists of an annular plenum, 16 injectors and an annular combustion chamber. Each injector consists of a burner and a perforated plate. Following [43], in the discrete model, the perforated plate and the burner are replaced by a cylindrical volume. Fig. 1 shows a section view of one sector of the numerical model of the MICCA combustor.

4.2. NURBS parametrization

Before generating the mesh, we decompose the geometry into the plenum, burner, perforated plate and combustion chamber. We start by defining the

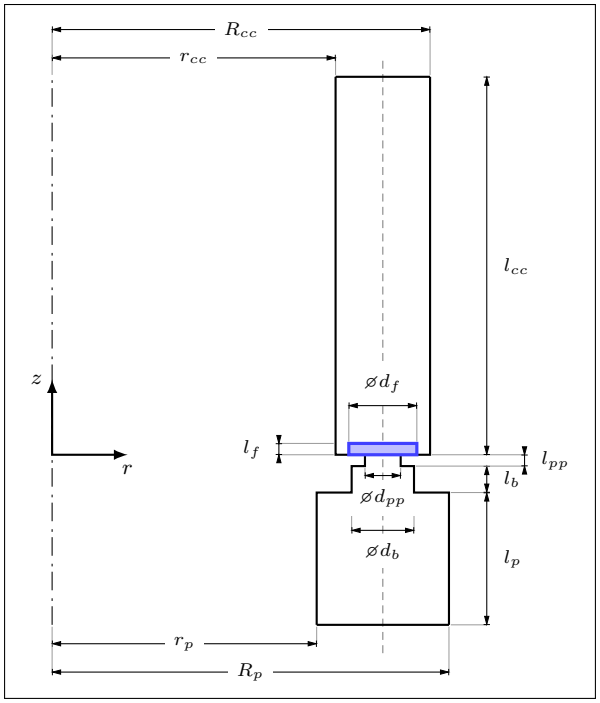

Figure 1: Section of one sector of the MICCA combustor. The dash-dotted line is the axis of symmetry. The subscripts stand for: plenum (p), burner (b), perforated plate (pp), flame (f), combustion chamber (cc). $r_p = 140$ mm, $R_p = 210$ mm, $l_p = 70$ mm, $d_b = 33$ mm, $l_b = 14$ mm, $d_{pp} = 18.9$ mm, $l_{pp} = 6$ mm, $d_f = 36$ mm, $l_f = 6$ mm, $r_{cc} = 150$ mm, $R_{cc} = 200$ mm, $l_{cc} = 200$ mm. The vertical dashed axis represents the longitudinal axis of the burner.

control points to generate the Non-Uniform Rational B-Spline (NURBS) surfaces. A brief introduction to NURBS using the example of a unit circle is in Appendix C.

We define 9 control points in the circumferential parametric direction, k_1, for each individual component. For the parametric radial direction, k_2, we use 5 control points for the plenum and combustion chamber and 3 control points for the burner and perforated plate. We use degree 2 B-Spline functions for the biparametric k_1 and k_2 directions. Then we generate inlet and outlet circles and a lateral boundary and fuse them to obtain a parametrized cylinder [44]. We iterate this process for each component. To generate the plenum and combustion chamber, we generate an inner cylinder with inner radius and subtract it from the outer cylinder with outer radius. To generate the burner and perforated plate for each sector, we copy the parametrized cylinders and rotate them 15 times. Finally, we merge the decomposed components to obtain the full geometry. The NURBS control points of the MICCA are shown in Fig. 2.

4.3. Numerical grid - Mesh

The parametrized geometry is then used to generate the unstructured mesh using the open-source automated 3D finite element mesh generator, Gmsh [45] with a Delaunay-triangulation method. We perform local mesh refinement near the reference points. We then optimize the quality of the tetrahedral elements using the Netgen optimizer. The unstructured mesh and the slice view of the sector mesh are shown in Fig. 3

4.4. Operating conditions and flame transfer function

We consider the same operating conditions as operating point B in [43]. A standing mode with a stable limit cycle at a frequency of 489 Hz is observed in the experiments. The equivalence ratio of the mixture of propane and air is $\phi = 1.11$. The total power of the flame for each burner is $\bar{\dot{Q}} = 2.08$ kW, and the bulk flow velocity is $\bar{u} = 0.66$ m/s. The ratio of specific heats, γ, is 1.4. The mean

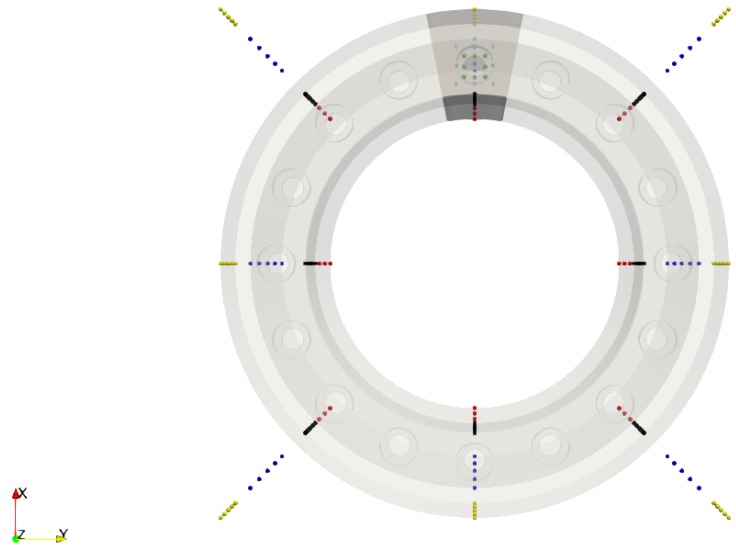

(a)

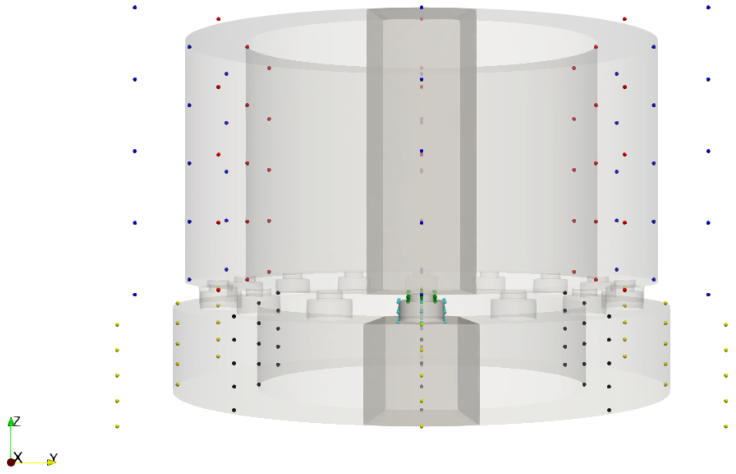

(b)

Figure 2: NURBS geometry viewed in the (a) XY-plane and (b) ZY-plane . The control points for each component are shown in different colors. The yellow and black control points control the outer and inner surfaces of the plenum, respectively. The green control points represent the burner, the cyan points indicate the perforated plate, and the blue and red points correspond to the outer and inner surfaces of the combustion chamber.

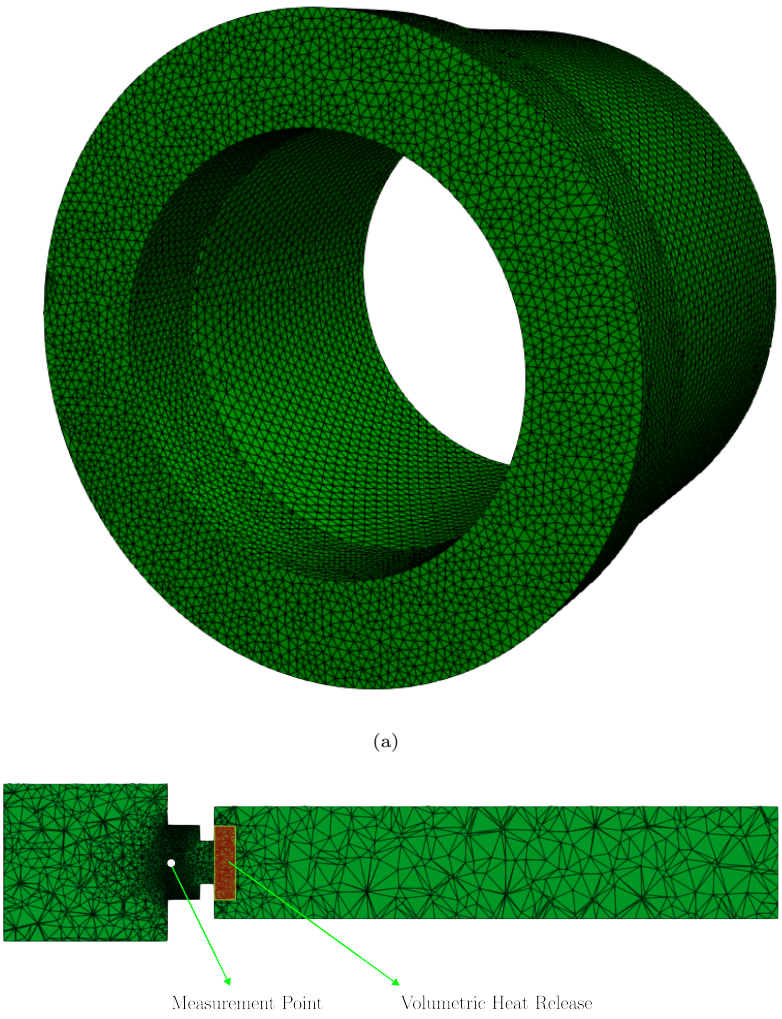

(a)

(b)

Figure 3: Finite element mesh of the MICCA combustor (a) external view and (b) slice through a burner. The grid consists of 5.4 million cells. Local refinement is applied at the measurement point to capture the gradient of the acoustic pressure there more accurately. The red zone shows the volumetric cylindrical heat release rate field.

temperature in the plenum and in the injectors is $\bar{T} = 300$ K. In the combustion chamber the temperature profile is parabolic, monotonically decreasing between the values at the flame position and the chamber outlet, shown in (35).

$$T(z) = \begin{cases} 300 & \text{if } z < z_f \\ (1200 - 1521)\left(\frac{z - z_f}{l_{cc}}\right)^2 + 1521, & \text{otherwise} \end{cases} \tag{35}$$

The experimental flame describing function (FDF) depends on the frequency of the excitation and on the ratio of the root mean square of the velocity fluctuation measured at the reference point, u', to the average flow velocity in the injector, $\bar{u}$.

We impose sound-hard (Neumann) acoustic boundary conditions at the combustor walls and impedance (Robin) boundary condition at the outlet boundary. The reflection coefficient we impose on the outlet boundary is $R_{outlet} = (Z_{outlet} - 1)/(Z_{outlet} + 1) = -0.875 - 0.2i$. It would be possible to model the flame with an amplitude-dependent flame describing function (FDF) and to obtain the shape sensitivity at each amplitude. In this paper, we demonstrate the method only for small amplitudes by obtaining the flame transfer function (FTF) from the FDF, by considering a small forcing amplitude, $|u'/\bar{u}| = 0.1$. In order to calculate the first derivative of the linear operator $\mathcal{L}$ with respect to the eigenvalue ω without approximations, we need $F(\omega)$ in equation (5) to be analytic in the complex plane [17]. We approximate the frequency response of the flame with a linear state-space model. The transfer function of the state-space model:

$$F(\omega) = \mathbf{c}^T \left(i\omega \mathbf{I} - \mathbf{A}\right)^{-1} \mathbf{b} + d \tag{36}$$

will correspond to the FTF. In order to obtain an analytic transfer function, we apply the Vector Fitting algorithm [46, 47, 48]. The experimental FTF and the transfer function of the state-space model are shown in Fig. 4.

5. Preliminary shape sensitivity analysis

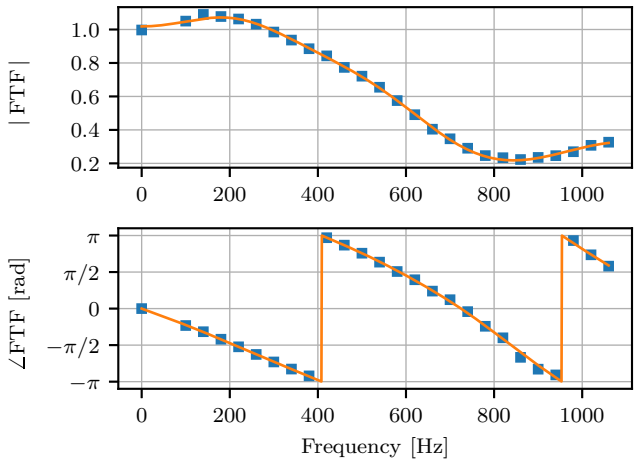

Figure 4: Gain and phase of the flame transfer function ($|u'/\bar{u}| = 0.1$) as a function of the frequency. The squares are the values obtained from the experiments [43], and the solid line is the transfer function of the linear state-space model, evaluated at real values of ω.

5.1. Shape sensitivity of degenerate modes

Because of the discrete rotational symmetry of the annular combustor, the modes are degenerate with algebraic and geometric multiplicity of 2. Consequently, these eigenvalues are referred to as semi-simple [8]. If this symmetry is broken, the eigenvalues split, and each can then be considered as a simple eigenvalue.

5.1.1. Shape derivatives for simple eigenvalues

In the case of simple eigenvalues, the shape gradient is the eigenvalue sensitivity to boundary perturbations. The shape derivative for a geometry perturbation proportional to the shape gradient constitutes an upper bound for the shape derivative itself. We obtain an upper bound for the angular frequency drift from the real part of G and for the growth rate drift from the imaginary part of G. In other words, shape changes proportional to the real part of the shape gradient have the maximum effect on the angular frequency, while shape changes proportional to the imaginary part of the shape gradient have the maximum effect on the growth rate.

5.1.2. Shape derivatives for semi-simple eigenvalues

In the case of semi-simple two-fold degenerate eigenvalues, the shape gradient, G_{ij}, has four entries and the shape derivatives are the eigenvalues of the matrix $\int CG_{ij}\,\mathrm{d}S$, where C is the perpendicular boundary perturbation or control point perturbation.

G_{11} gives the upper bound for ω_1 and G_{22} gives the upper bound for ω_2. For geometry perturbations proportional to G_{12} and G_{21}, either their real or imaginary parts, the diagonal elements of the matrix $\int CG_{ij}\,\mathrm{d}S$ are equal to zero. Therefore, the shape derivatives take the form $\omega' = \pm(a + bi)$. The shape derivative is the same for the two eigenvalues, ω_1 and ω_2, but with opposite sign. In other words, at first order the eigenvalues split in opposite directions. The off-diagonal elements also have the property that:

$$\int G_{ij}\,\mathrm{d}S = 0 \quad \text{if } i \neq j \tag{37}$$

which means that the volume of the combustor does not change when boundary perturbations proportional to them are applied. Interestingly, this is conceptually similar to what was observed by Mensah [17] for the same annular combustor, when the burners/injectors are perturbed such that the FTF perturbations have the same phase and their average is zero. The eigenvalue perturbation for the two modes is the same but with opposite sign.

5.1.3. Shape differentiability

In the simple case, the eigenvalues are shape differentiable; i.e. the derivative $\mathrm{d}\omega(\Omega)$ exists for all directions $\boldsymbol{V}$ and the mapping $\boldsymbol{V} \mapsto \mathrm{d}\omega(\Omega)$ is linear and continuous. In the semi-simple degenerate case, the eigenvalues are not differentiable at first order because each eigenvalue splits in two. This can cause a problem in gradient-based optimization because the gradients are in general discontinuous and the cost functional is therefore non-convex. This problem can be avoided by applying symmetry-preserving geometry changes. In this case, the two repeated eigenvalues do not split and the two shape derivatives have the same value. Sections 6.1 and 6.2 concern this type of geometry change. When

applying symmetry-breaking changes, this problem can be worked around by noticing when an eigenvalue has split and subsequently calculating the shape derivatives of each split eigenvalue separately. Section 7 concerns this type of geometry change. In all cases, the real part of the shape derivative represents changes that reduce the angular frequency and the imaginary part represents changes that reduce the growth rate.

5.2. Shape modification

In this paper, we consider changes to the plenum and combustion chamber. We can also compute shape derivatives for changes to the diameter of the burner and to the total flow passage area of the perforated plate. Such changes would, however, alter the flame's transfer function. We have used an experimentally-derived flame transfer function and we do not know how it would change due to these changes, so we do not consider these changes further. For an estimate of flame transfer function changes in a different burner, the reader is referred to [13].

In this paper we propose two different shape perturbation methods: perpendicular boundary perturbations and NURBS control point perturbations. In the former, the displacements along the boundary's normal direction are uniform. In the latter, the displacements along the boundary's normal direction are non-uniform due to the independent movements of individual control points. We apply both of these methods and demonstrate the shape changes for two different degenerate modes in Sec. 6.1 and Sec. 6.2. In Sec. 7, we consider symmetry-breaking changes for the mixed mode using the shape gradients calculated at the NURBS control points.

5.2.1. Perpendicular boundary perturbations

When using a non-parametric approach, the boundary displacement is proportional to the shape gradient. We divide the geometry into patches and, for each patch we use Eq. (34) to compute the shape derivatives for a unitary

deformation field

$$C = \begin{cases} 1 & \text{on } \partial\Omega_i \\ 0 & \text{elsewhere} \end{cases} \tag{38}$$

Then we divide the shape derivatives by the surface area of the patch. In this way, we obtain a local average of the derivatives, which does not depend on the area of the patch. An example perpendicular deformation field, C, is shown in Fig. 5 for the outer surface of the combustion chamber.

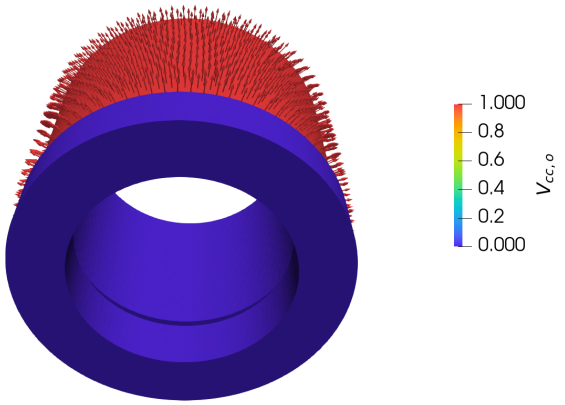

Figure 5: Perpendicular deformation field ($\boldsymbol{V}$) for the outer combustion chamber surface of the MICCA combustor. By construction, the deformation vectors have the same magnitude at each node of the surface mesh.

5.2.2. Control point perturbations

When using a parametric approach, as in the case of B-spline or NURBS surfaces, the set of admissible boundary displacements and shapes is expanded. We point out that more elaborate shape changes could be considered with this approach, as we obtained the NURBS parametrization of the shape. However, for this approach, we do not change the length of the plenum and the combustion chamber. The control point perturbation, $\boldsymbol{V}_{i,j}$, is the derivative of the NURBS

surface with respect to the position of the control point $\boldsymbol{P}_{i,j}$. We use

$$\boldsymbol{V}_{i,j} = \frac{\partial S(k_1, k_2)}{\partial \boldsymbol{P_{i,j}}} = \frac{\sum_{i=0}^{m}\sum_{j=0}^{m} N_{i,p}(k_1)N_{j,q}(k_2)w_{i,j}}{\sum_{i=0}^{m}\sum_{j=0}^{m} N_{i,p}(k_1)N_{j,q}(k_2)w_{i,j}} \tag{39}$$

to compute the corresponding deformation fields for the node i in the circumferential direction and the node j in the axial direction. In Eq. (39), N denotes the B-Spline basis function, k_1 and k_2 denote the circumferential and axial parameters of the surface and $w_{i,j}$ denotes the weight of the control point $\boldsymbol{P}_{i,j}$. We show the boundary perturbation of the control point on the plenum surface in Fig. 6.

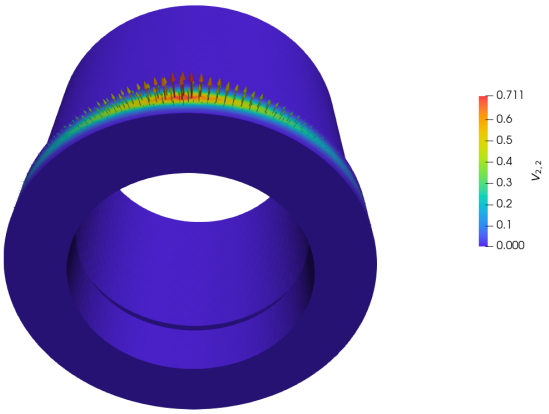

Figure 6: Deformation field ($\boldsymbol{V}$) due to changes in the middle node on the top of the lateral plenum surface of the MICCA combustor.

As we only perform changes on the plenum and combustion chamber, we use Eq. (28) to compute the shape gradients of the control points on the Neumann boundaries. We apply two different geometry modifications using NURBS control points: symmetry-preserving (Sec. 6) and symmetry-breaking (Sec. 7).

5.3. Optimization procedure

When we modify the shape, we fix the geometry of the burner and allow changes only in the plenum and in the combustion chamber. For symmetry-

preserving changes, the combustor axis in the longitudinal direction is taken as the symmetry axis. Our goal is to reduce the eigenvalue growth rate by following the steps below.

(i) We use P2 elements to compute the shape derivatives for each boundary or control point.

(ii) We take the imaginary part and normalize such that the maximum absolute value among all the shape derivatives is 1.

(iii) We subtract from the geometric parameters the imaginary part of the shape derivatives multiplied by the step size, ϵ, which can take a range of values. Here, ϵ is 0.025 for symmetry-preserving changes and between 0.01 and 0.07 for symmetry-breaking changes.

(iv) We generate a refined finite element mesh with latterly calculated geometric parameters.

(v) We simulate the optimized geometry with P1 elements and observe the changes in the growth rate of the new eigenvalue of the new eigenmode.

6. Symmetry-preserving Changes

In this section, we change geometries of the plenum and the combustion chamber with two methods: perpendicular boundary movements and control point displacements with symmetry-preserving changes.

6.1. Azimuthal Mode

Fig. 7 shows the normalized magnitude of the eigenvector, $\hat{p}$ of the first azimuthal mode. Figure 8 shows the real and the imaginary part of the shape derivatives for the plenum and the combustion chamber. These are shown as perpendicular boundary displacements proportional to the shape derivatives of the surfaces of the combustor. In order to investigate the effects of the control points on the lateral boundaries of the plenum and combustion chamber, the shape derivatives of the control points on the $+yz$ plane ($k_2 = 2$) are computed. Figure 9 shows the real and the imaginary part of the shape derivatives for the

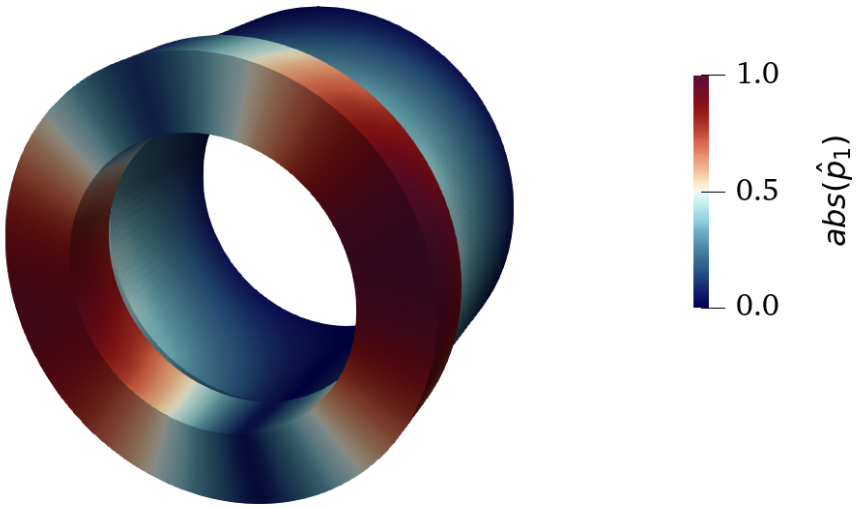

Figure 7: Normalized absolute value of the eigenvector, $\hat{p}$, of the first azimuthal mode of the MICCA combustor (in arbitrary units). This is a weakly coupled plenum mode. The associated eigenvalue is $\omega = 3222 + 517i$ rad s^{-1}.

first azimuthal mode. These are shown as control point displacements proportional to the shape derivatives in the normal direction of the relevant surface. Fig. 10 (top) shows the initial and the final shapes of a sector of the annular combustor. The growth rate has reduced by 20% after 4 iterations. Although the process can be continued, the salient points are most easily demonstrated before the geometry has changed significantly. Table 1 tabulates the associated eigenvalues for the initial geometry and the two final geometries. The size of the

Table 1: Degenerate eigenfrequencies of the MICCA combustor for the initial and the two optimized designs. The units of the eigenfrequencies are in rad s^{-1}. The eigenvalues for each case get closer as number of cells increase (not shown here).

Case	$\omega_{1,r}$	$\omega_{1,i}$	$\omega_{2,r}$	$\omega_{2,i}$	$\angle\hat{q}$ - $\angle\hat{p}$ [deg]
initial	3222.77	517.51	3222.50	518.66	56.83
perpendicular	3085.27	402.92	3084.97	401.03	65.37
NURBS	3152.32	413.42	3152.19	414.30	62.10

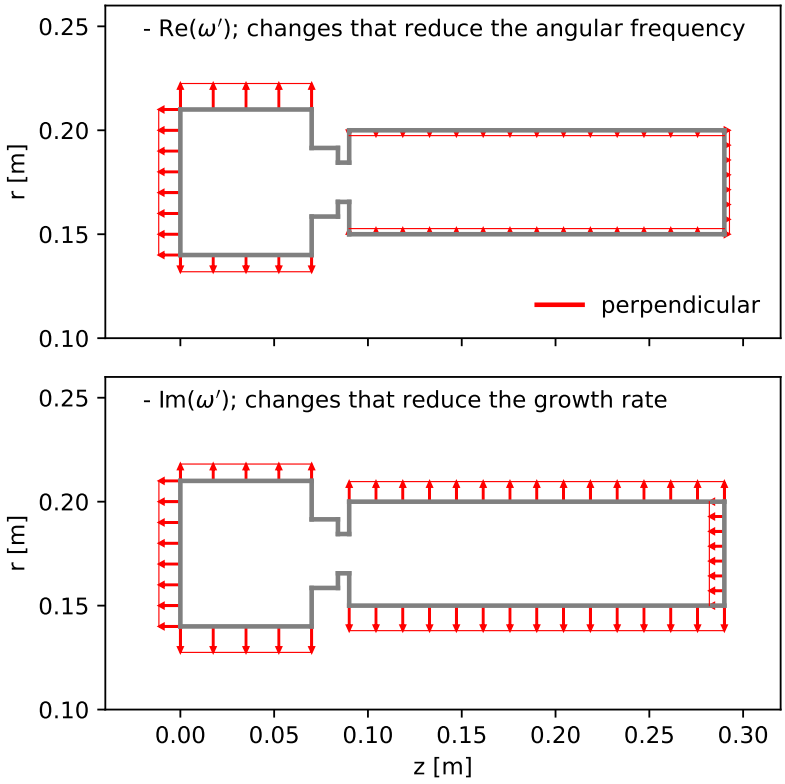

Figure 8: Real (top) and imaginary (bottom) components of the eigenvalue shape derivatives for changes to the length and the radii of the plenum and the combustion chamber for the first azimuthal mode. The real part gives the influence on the angular frequency and the imaginary part gives the influence on the growth rate.

plenum has increased for both approaches. The only boundary that has moved inwards is the combustion chamber outlet with perpendicular displacements. Fig. 10 (bottom) shows the modulus of the corresponding pressure eigenvectors along the dotted line at $r = 0.175$ m, where the absolute value of the eigenvector is maximum.

We observe that changes applied to the shape of the combustion chamber have little or no effect on the angular frequency, which is expected because this mode is a plenum mode. We also observe that the sensitivity of the eigenvalue

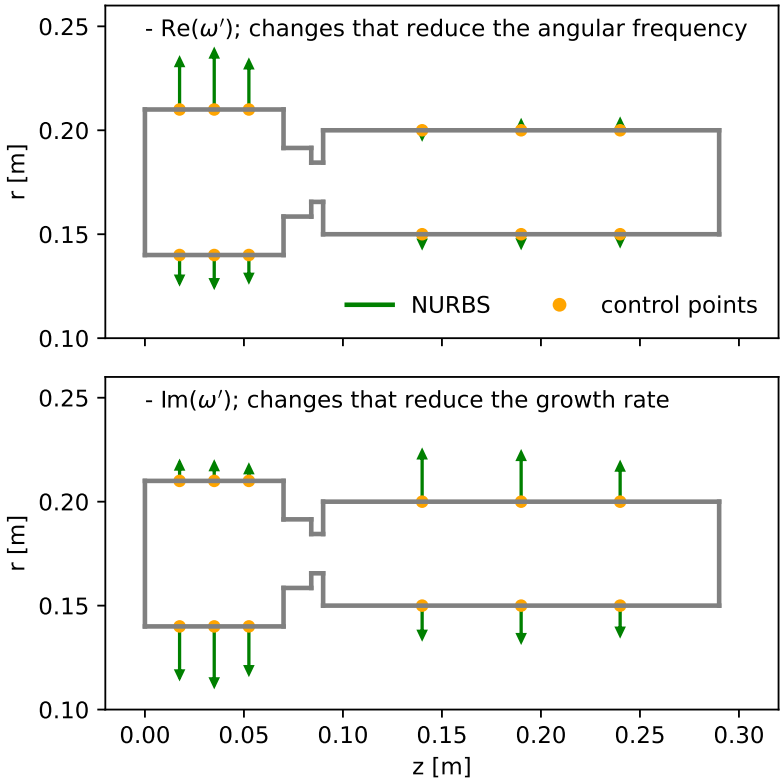

Figure 9: As for Fig. 8 but for changes parametrized by the NURBS points.

growth rate in the plenum is higher than in the combustion chamber. This can be explained by the fact that the gas is cooler, so the local wavelength is shorter and therefore geometry modifications of a given size have more influence.

6.2. Mixed Mode

In this subsection, we find an unstable mixed tangential–longitudinal thermoacoustic eigenmode of the MICCA. We perform shape sensitivity analysis for this eigenmode and we reveal the optimized designs using perpendicular surface changes and control point movements with symmetry-preserving changes. Fig. 11 shows the absolute value of the eigenvector of the mixed mode. The corresponding eigenfrequency is 1663.60 Hz with 377.19 rad s^{-1} growth rate.

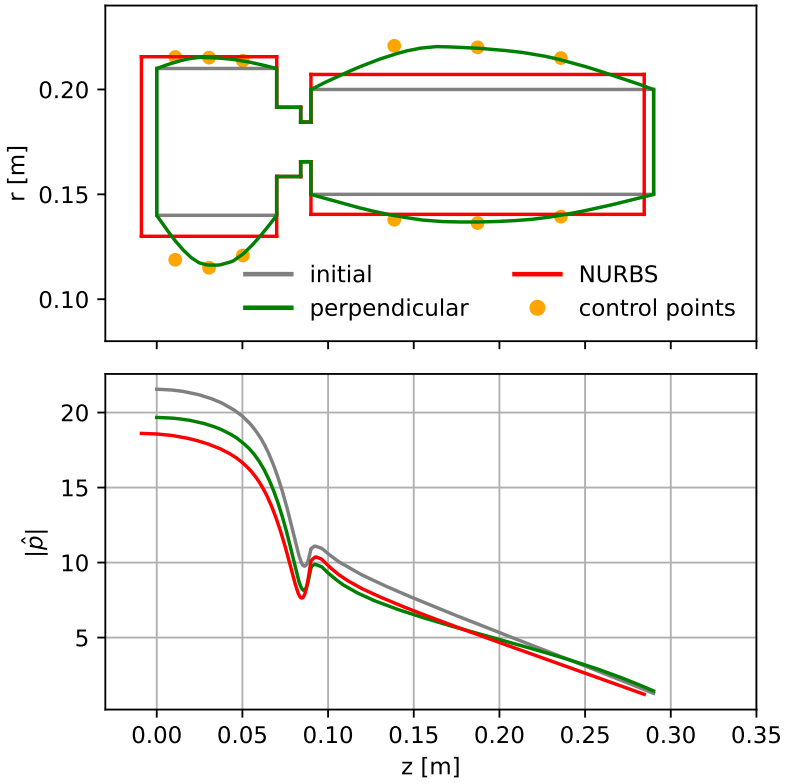

Figure 10: (Top) Section view of one sector of the MICCA combustor for the initial (black), perpendicular displacement (red) and the NURBS displacement (green) after applying the shape changes to the plenum and the combustion chamber to reduce the growth rate. The gray dashed line represents the longitudinal axis of the burner as shown in Fig. 1. (Bottom) Absolute value of the eigenvector of the first azimuthal mode of the MICCA combustor, along the dotted line in the top figure, before (gray) and after (red and green) the shape changes. The sector is that in which the pressure is maximum.

Figure 12 shows the real and the imaginary part of the shape derivatives for the plenum and the combustion chamber for the mixed mode. These are shown as perpendicular boundary movements proportional to the shape derivatives of the surfaces of the combustor. Figure 13 shows the real and the imaginary part of the shape derivatives for the unstable mixed mode. The shape derivatives of the control points on the $+xz$ plane ($k_2 = 0$) are computed. These are depicted as

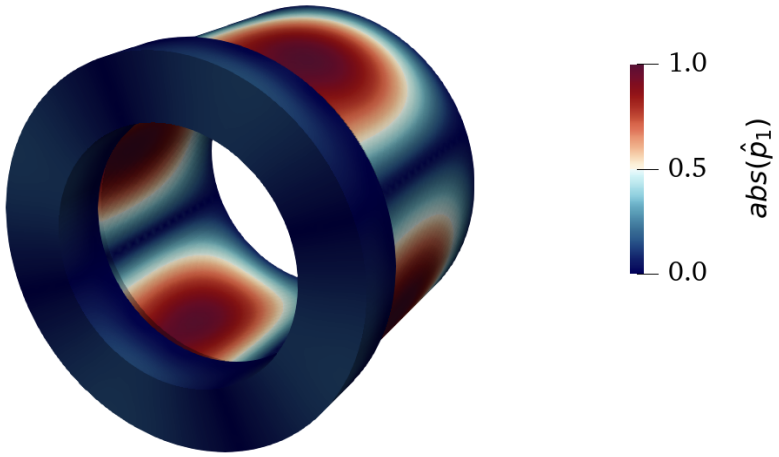

Figure 11: Normalized magnitude of the eigenvector of the mixed mode. The associate eigenvalue is $\omega = 10830.42 + 401.16i$ rad s^{-1}.

control point displacements proportional to the shape derivatives in the outward normal direction of the combustor boundary. Fig. 14 (top) shows the initial and the final shapes of a sector of the annular combustor. The most influential region on the growth rate is found to be the combustion chamber for the mixed mode. This is because the circumferential and axial modes combine in the combustion chamber. The contribution of the axial component of the mixed mode causes higher sensitivity on the outlet surface because it depends on the length of the combustion chamber. Table 2 tabulates the associated eigenvalues for the initial geometry and the optimized geometries. The same step size, 0.025 is chosen to perform shape changes with control points or boundary displacements. After 4 iterations, the growth rate has reduced by 32% with perpendicular boundary changes and 47% with control point displacements. The NURBS approach provides more stabilization for this unstable mixed mode considering same step size.

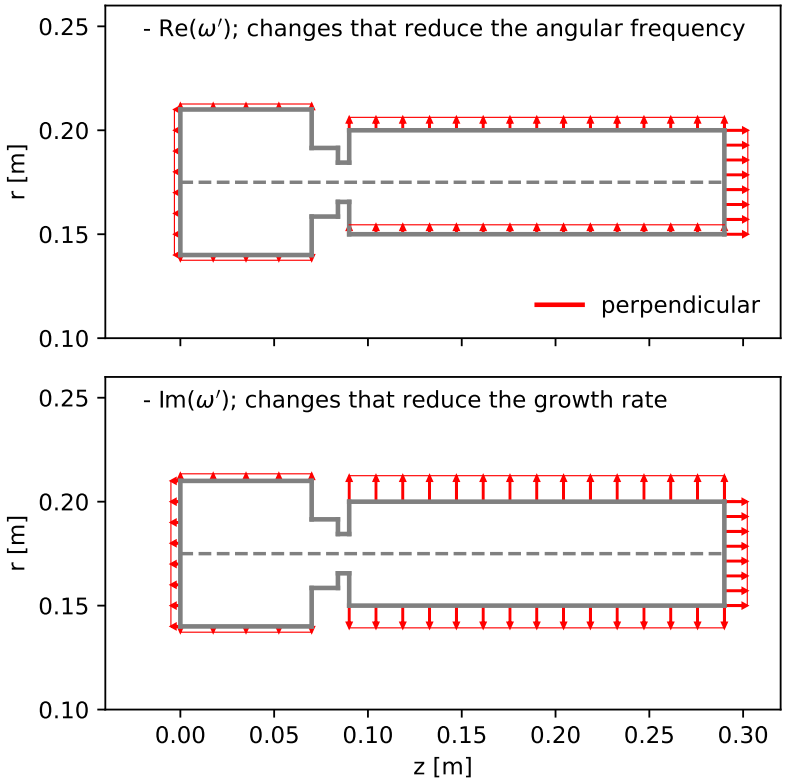

Figure 12: As for Fig. 8 but for the mixed mode.

6.3. Dephasing mechanism

The physical mechanism behind the growth rate's reduction can be explained by using the (generalized) Rayleigh criterion. According to the Rayleigh criterion, a thermoacoustic system is unstable if the average of the product between the pressure, p', and the heat release rate perturbation, $\dot{q}'$, over the volume and over one period of oscillation is greater than the average of the losses due to acoustic radiation from the boundaries, Eq. (B.2). This paper focuses only on shape sensitivity of eigenvalues with Neumann and Robin boundary conditions. Internal acoustic losses could be included, but this would not change the analysis regarding shape sensitivity of eigenvalues. If we expand the Rayleigh index, $p'\dot{q}'$, we see that it depends on the modulus of the pressure in the flame

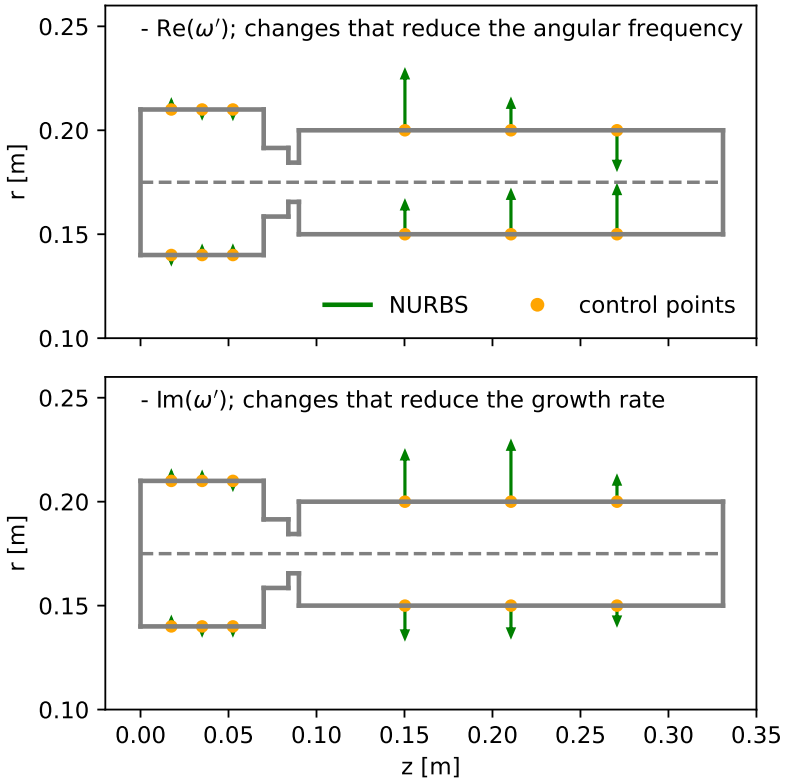

Figure 13: As for Fig. 9 but for the mixed mode.

volume, $|\hat{p}|$, and of the component of the velocity along the reference direction at the reference point, $|\hat{\boldsymbol{u}}(\boldsymbol{x}_r) \cdot \boldsymbol{n}_r|$, and on the phase angle difference between the heat release rate perturbation and the pressure perturbation as well as on the modulus of the flame transfer function. If we expand the acoustic energy flux, $p'\boldsymbol{u}'$, we see that this only depends on the modulus of the pressure at the boundary. On the other hand, the last columns of Table. 1 and Table 2 show the averaged phase difference between the fluctuating heat release rate and the pressure perturbation for all sixteen burners for the azimuthal mode and the mixed mode, respectively. To calculate the phase of the heat release fluctuations we use (5) to obtain $\hat{q}$. The phase of the acoustic pressure can be directly obtained from the calculated eigenvector, $\hat{p}$. For each burner we pick the centre

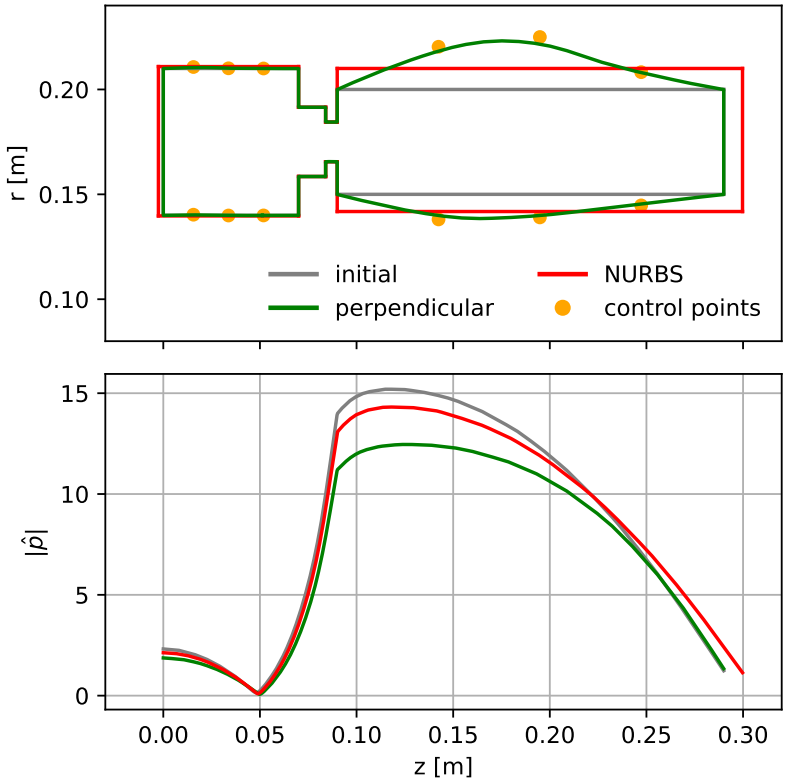

Figure 14: As for Fig. 10 but for the mixed mode.

point of the heat release zone (Fig. 3b) and calculate the phase angles of $\hat{q}$ and $\hat{p}$ at that point, then take the difference to obtain the phase difference.

We see from Table 1 and Table 2 that, by changing the geometry, the algorithm increases the phase difference between the pressure, $\hat{p}$, and the heat release rate, $\hat{q}$. This reduces the heat converted to work each cycle and therefore reduces the growth rate of the system (B.6). In this process the pressure within the flame volume and the velocity along the reference direction at the reference point do not change. They would change, however, if we were to allow the shape of the injector to change. In [13], the alterations in bluff body geometry are taken into account, showing that even minor changes yield a substantial influence on the flame transfer function, ultimately impacting the stability of

Table 2: Degenerate eigenfrequencies of the mixed mode for the initial and the two optimized designs. The units of the eigenfrequencies are in rad s^{-1}. N_c denotes the number of finite element cells for each case. The eigenvalues for each case get closer as N_c increases (not shown here).

Case	$\omega_{1,r}$	$\omega_{1,i}$	$\omega_{2,r}$	$\omega_{2,i}$	N_c	$\angle\hat{q}$ - $\angle\hat{p}$ [deg]
initial	10830.42	401.16	10831.18	402.10	13.60M	-15.94
perpendicular	10552.63	274.20	10552.97	274.83	11.78M	-19.70
NURBS	10322.15	211.83	10322.04	211.76	11.74M	-23.73

the thermoacoustic system. Similarly, the algorithm would try to decouple the plenum and the combustion chamber by expanding the diameter of the burner, d_b, and contracting the diameter of the perforated plate, d_{pp}. Consequently it would reduce the modulus of the velocity perturbation at the reference point and of the pressure perturbation within the flame volume.

This analysis shows how to significantly alter the growth rate of thermoacoustic oscillations by changing the geometry of a combustion chamber and plenum. In most practical devices, it would be possible to alter the geometry of the plenum without extensive re-design. It would be less feasible to alter the geometry of the combustion chamber, which is constrained by other considerations such as cooling and high altitude re-light. Nevertheless, as seen here and in [13], the most influential component is the burner, due to its effect both on the flow rate through the burner and the heat release rate response of the flame.

7. Symmetry-breaking Changes

In this section, we consider non-axisymmetic changes in the MICCA geometry for the unstable mixed mode. Compared to axisymmetric changes in Sec. 6, we enlarge the deformation step size, ϵ, to enhance geometry deformation and better observe the effects of non-axisymmetry. Each control point of the NURBS geometry is moved in the direction provided by its shape derivative. The resulting eigenvectors can be seen in Fig. 15. We observe that the

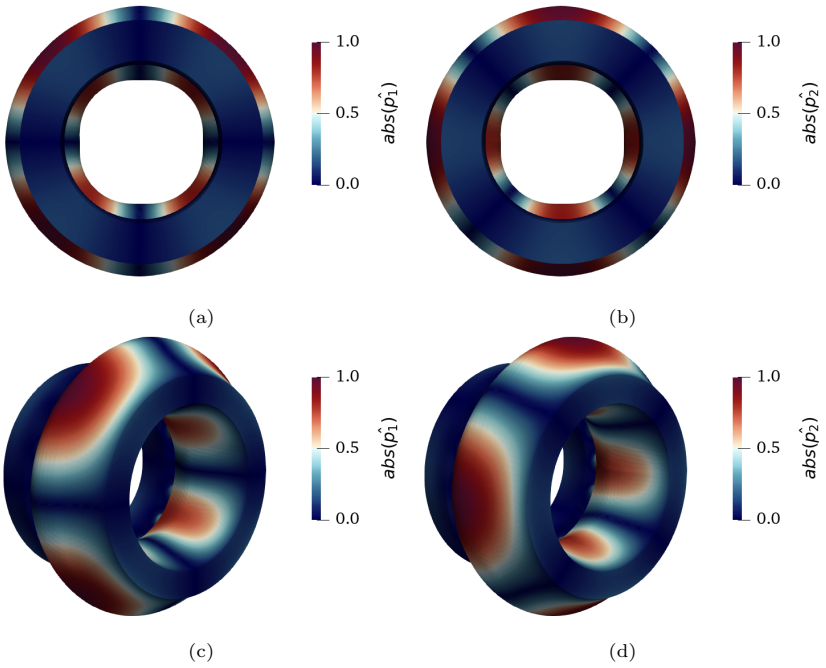

Figure 15: Normalized magnitude of the mixed mode eigenvectors of the non-axisymmetrically deformed MICCA for $\epsilon = 0.07$. The associate eigenvalues are $\omega_1 = 9709.58 + 100.72i$ rad s^{-1} (left column) and $\omega_2 = 9465.52 + 101.27$ rad s^{-1} (right column).

NURBS geometry is extended more in the outward normal direction of the control points on the pressure node of the first mixed eigenmode, $\hat{p}_1$. Due to the non-axisymmetric changes in the NURBS geometry, eigenvalue degeneracy is lost during symmetry-breaking changes.

From Fig 16, eigenvalue splitting is observed between two unstable mixed modes for different deformations. The changes in the eigenvalues follow two different branches. Starting from the degenerate case where $\epsilon = 0$, the non-axisymmetric changes split both angular frequencies and growth rates. For each deformation case, the magnitude of the frequency splits are much greater than those of the growth rate. For the most deformed case ($\epsilon = 0.07$), the frequency difference between the two unstable modes reaches 244.06 rad s^{-1} whereas the growth rate varies by 0.55 rad s^{-1}.

As we follow the deformation directions provided by the shape derivatives,

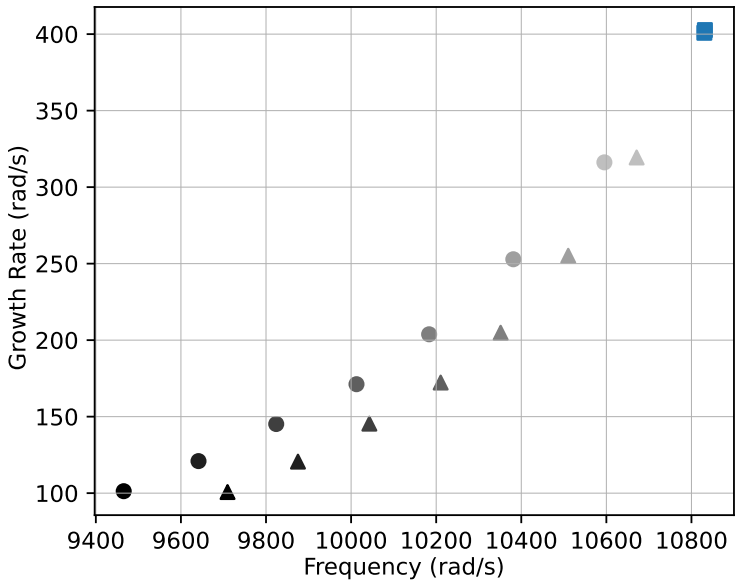

Figure 16: Splitted eigenvalues of the $\hat{p}_1$ (triangles) and $\hat{p}_2$(circles) for different deformation sizes (ϵ). Blue square marker represents the degenerate configuration before perturbation. The lightest grey corresponds to $\epsilon_0 = 0.01$ and the darkest to $\epsilon_7 = 0.07$. Same triangle-circle couples correspond same deformation size.

the splitted modes become more stable as expected, compared to the initial geometry. When compared to the axisymmetric deformations with the same deformation size ϵ, one mode becomes more stable and other mode becomes less stable for symmetry-breaking modifications in the geometry.

8. Conclusions

We combine a thermo-acoustic Helmholtz solver with adjoint-based shape optimization to reduce the growth rate of linearly unstable thermoacoustic modes in a symmetric annular combustor. We parametrize the entire combustor geometry with NURBS control points. The modes are azimuthal and mixed, and therefore two-fold degenerate. We express the shape derivative of the eigenvalue in Hadamard form, i.e. for arbitrary shape changes. We ap-

ply both symmetry-preserving and symmetry-breaking changes to the MICCA geometry with NURBS and show that these can be used to reduce the thermoacoustic growth rate efficiently. This process could be continued to zero growth rate, but large geometry changes would be required. After modifying the shape, we use the analysis to reveal the physical mechanism that causes the growth rate's reduction. The shape changes increase the phase difference between the pressure and the heat release rate fluctuations.

This method can be applied to the plenum, the burner, and the combustion chamber. In practical devices, modifying the plenum may be the most practical option and, as shown in this paper, has a strong influence on the thermoacoustic growth rate. The most influential component on thermoacoustic behaviour, however, is the burner. We use an experimentally-determined flame transfer function, which is fixed because we do not know how it would change with the burner geometry. If adjoint methods are to be used for combustor design, then these methods must include the influence of the burner shape on the flow behaviour, as in [49], and hence on the flame. Using the linearized Navier-Stokes equations as in [50] with resolvent analysis would provide a better approximation to the response of the flame and enable a deeper exploration of the influence of burner geometry on thermo-acoustic oscillations. This is a significantly larger challenge and we leave it for future work.

The methods in this paper can now be applied to more complex geometries such as those on aircraft gas turbines, in which the plenum surrounds the combustion chamber and is connected to it by dilution holes. While this paper addresses the conceptual challenges of obtaining shape gradients of thermoacoustic eigenvalues, the implementation of NURBS in realistic systems introduces significant geometric complexity. Additionally, modeling the inlet and outlet conditions of aero-engine combustors remains challenging, particularly due to choked flow near the compressor and the turbine, and is out of scope of this paper. Finally, we note that it is possible to reduce the growth rates of several eigenvalues simultaneously, as in [13], although this has not been attempted in this paper.

Acknowledgements

We are grateful to Davide Laera for providing us the data of the MICCA combustor. Ekrem Ekici acknowledges funding from Türkiye's Ministry of National Education. Stefano Falco acknowledges the European Union's Framework Programme for Research and Innovation Horizon 2020 under the Marie Skłodowska Curie grant agreement ANNULIGhT No 765998.

Appendix A. Tangential calculus

Let f be a scalar field and $\boldsymbol{v}$ a vector field. The tangential gradient of f is

$$\boldsymbol{\nabla}_\Gamma f = \boldsymbol{\nabla} f - \frac{\partial f}{\partial n}\boldsymbol{n} \tag{A.1}$$

This is the orthogonal projection of the gradient onto the tangent space. The tangential divergence of $\boldsymbol{v}$ is

$$\mathrm{div}_\Gamma \boldsymbol{v} = \mathrm{div}\boldsymbol{v} - (D\boldsymbol{v}\boldsymbol{n})\cdot\boldsymbol{n} \tag{A.2}$$

$D\boldsymbol{v}$ is the Jacobian of $\boldsymbol{v}$ and $D\boldsymbol{v}\boldsymbol{n}$ is the matrix product between $D\boldsymbol{v}$ and $\boldsymbol{n}$. In addition to the definitions of tangential gradient and divergence, we give the Tangential Stokes formula

$$\int_\Gamma f\mathrm{div}_\Gamma \boldsymbol{v} + \nabla_\Gamma f\cdot\boldsymbol{v}\,\mathrm{d}S = \int_\Gamma \kappa f\boldsymbol{v}\cdot\boldsymbol{n}\,\mathrm{d}S \tag{A.3}$$

where $\kappa = \mathrm{div}_\Gamma \boldsymbol{n}$ is the curvature.

Appendix B. Acoustic energy balance

If we take $\bar{\rho}\boldsymbol{u}'\cdot(1\mathrm{a}) + \frac{1}{\gamma\bar{p}}(1\mathrm{b})$, we obtain

$$\frac{\partial e'}{\partial t} + \boldsymbol{\nabla}\cdot(p'\boldsymbol{u}') = \frac{\gamma-1}{\gamma\bar{p}}p'\dot{q}' \tag{B.1}$$

where $e' = \bar{\rho}\boldsymbol{u}'^2/2 + \frac{1}{\gamma\bar{p}}p'^2/2$ is the acoustic energy density and $p'\boldsymbol{u}'$ is the acoustic energy flux [51]. If we average over the volume and over one period, we obtain the stability criterion

$$\frac{\gamma-1}{\gamma\bar{p}}\int_\Omega\int_0^T p'\dot{q}'\,\mathrm{d}V\,\mathrm{d}t > \int_{\partial\Omega}\int_0^T p'\boldsymbol{u}'\cdot\boldsymbol{n}\,\mathrm{d}S\,\mathrm{d}t \tag{B.2}$$

p', $\boldsymbol{u}' \cdot \boldsymbol{n}$ and q' can all be written, as in Eq. (3), in the form

$$(\cdot)'(\boldsymbol{x}, t) = \left|\hat{(\cdot)}(\boldsymbol{x})\right| \cos\Big(2\pi f t - \angle\hat{(\cdot)}(\boldsymbol{x})\Big) e^{\lambda t} \tag{B.3}$$

where f and λ are the frequency and the growth rate of the eigenvalue, $\omega = 2\pi f + i\lambda$, respectively, and $\angle\hat{(\cdot)}$ is the phase angle. Before substituting the expressions for p', $\boldsymbol{u}' \cdot \boldsymbol{n}$ and $\dot{q}'$ into (B.2), we write the trigonometric identity

$$\cos(2\pi f t - \angle\hat{p}) \cos(2\pi f t - \angle\hat{q}) = \frac{1}{2}\big[\cos(4\pi f t - \angle\hat{p} - \angle\hat{q}) + \cos(\angle\hat{q} - \angle\hat{p})\big] \tag{B.4}$$

Equation (B.2) becomes

$$\frac{\gamma - 1}{\gamma \bar{p}} \int_\Omega |\hat{p}||\hat{q}| \cos(\angle\hat{q} - \angle\hat{p}) \,\mathrm{d}V \;>\; \int_{\partial\Omega} |\hat{p}||\hat{\boldsymbol{u}} \cdot \boldsymbol{n}| \cos(\angle\hat{\boldsymbol{u}} \cdot \boldsymbol{n} - \angle\hat{p}) \,\mathrm{d}S \tag{B.5}$$

In fact, the integral containing $\cos(4\pi f t - \angle\hat{p} - \angle\hat{q}) e^{2\lambda t}$ is zero, regardless of the values assumed by the two phase angles (and analogously the integral containing $\cos(4\pi f t - \angle\hat{p} - \angle\hat{\boldsymbol{u}} \cdot \boldsymbol{n}) e^{2\lambda t}$). We substitute $\hat{q}$ from Eq. (5) and $\hat{\boldsymbol{u}} \cdot \boldsymbol{n}$ from Eq. (8) into Eq. (B.5), and obtain

$$(\gamma - 1) \frac{\bar{q}}{\bar{u}} |F(\omega)| \int_\Omega |\hat{p}||\hat{\boldsymbol{u}}(\boldsymbol{x}_r) \cdot \boldsymbol{n}_r| \cos(\angle\hat{q} - \angle\hat{p}) \,\mathrm{d}V > \int_{\partial\Omega} \frac{\bar{c}}{|Z|} \big|\hat{p}^2\big| \cos(\angle Z) \,\mathrm{d}S \tag{B.6}$$

The left-hand side depends on the modulus of the flame transfer function, of the pressure in the flame volume and of the component of the velocity along the reference direction at the reference point, and on the phase angle difference between the heat release rate perturbation and the pressure perturbation. The right-hand side only depends on the modulus of the pressure at the boundary if we assume that the impedance does not depend on the frequency.

Appendix C. NURBS representation of unit circle

In this appendix, we give a brief introduction to NURBS curves and surfaces with a unit circle example. The main reference for this section is chapter 7 in

[44]. A NURBS curve with degree p can be obtained from

$$C(k_1) = \frac{\sum_{i=0}^{n} N_{i,p}(k_1) w_i \boldsymbol{P_i}}{\sum_{i=0}^{n} N_{i,p}(k_1) w_i} \tag{C.1}$$

where $\boldsymbol{P_i}(x_i, y_i, z_i)$ are the control points, w_i are the weights, $N_{i,p}$ are the pth degree B-spline basis functions and k_1 is the knot. Composition of two NURBS curves with different directions gives a NURBS surface. The mathematical representation of the NURBS surface is similar to (C.1):

$$S(k_1, k_2) = \frac{\sum_{i=0}^{n} \sum_{j=0}^{n} N_{i,p}(k_1) N_{j,q}(k_2) w_{i,j} \boldsymbol{P_{i,j}}}{\sum_{i=0}^{n} \sum_{j=0}^{n} N_{i,p}(k_1) N_{j,q}(k_2) w_{i,j}} \tag{C.2}$$

where q is the degree and the k_2 is the knot of the second curve.

For shape derivative calculations, we need displacement fields from NURBS. We can obtain these by differentiating the NURBS geometry with respect to the control point, giving:

$$\boldsymbol{V}_i = \frac{\partial C(k_1)}{\partial \boldsymbol{P_i}} = \frac{\sum_{i=0}^{n} N_{i,p}(k_1) w_i}{\sum_{i=0}^{n} N_{i,p}(k_1) w_i} \tag{C.3}$$

for the curve and

$$\boldsymbol{V}_{i,j} = \frac{\partial S(k_1, k_2)}{\partial \boldsymbol{P_{i,j}}} = \frac{\sum_{i=0}^{n} \sum_{j=0}^{n} N_{i,p}(k_1) N_{j,q}(k_2) w_{i,j}}{\sum_{i=0}^{n} \sum_{j=0}^{n} N_{i,p}(k_1) N_{j,q}(k_2) w_{i,j}} \tag{C.4}$$

for the surface. Note that Eq. (C.4) implies the cross product of the basis functions of the two different NURBS curves. We use these formulae to calculate the displacement field in the shape gradient formula.

Appendix C.1. NURBS Parametrization of Unit Circle

As a demonstration, we define a unit circle using NURBS. Parameters of the NURBS control points are tabulated in Table C.3. Using Gmsh Python

Table C.3: Control points and their weights of the NURBS for the unit circle ($r = 1$) with degree 2. The knot vector is $k_1 = (0, 0, 0, 0.25, 0.25, 0.5, 0.5, 0.5, 0.75, 0.75, 1, 1, 1)$.

i	x_i	y_i	z_i	w_i
1	1.0	0.0	0.0	1.0
2	1.0	1.0	0.0	$\sqrt{2}/2$
3	0.0	1.0	0.0	1.0
4	-1.0	1.0	0.0	$\sqrt{2}/2$
5	-1.0	0.0	0.0	1
6	-1.0	-1.0	0.0	$\sqrt{2}/2$
7	0.0	-1.0	0.0	1.0
8	1.0	-1.0	0.0	$\sqrt{2}/2$
9	1.0	0.0	0.0	1.0

API, we define the control points in Table C.3 with the weights of the control points and the knot vector with multiplicities as well as characteristic mesh size of 0.04. We then generate the degree 2 closed NURBS curve and transform it into the NURBS surface to obtain the NURBS unit circle. If we deform point 2 in the direction towards the centre of the circle, we obtain the deformed circle shown in Fig. C.17. The parametrization utility of the Gmsh model is used to parametrize the boundary curve. We use these parameters to compute the displacement field of the control points using Eq. (C.3) to compute the pointwise shape derivative in the outward normal direction. The example displacement field of the second control point of the unit circle is shown in Fig. C.18.

References

[1] L. Rayleigh, The Explanation of Certain Acoustical Phenomena, Nature 18 (455) (1878) 319–321. doi:10.1038/018319a0.

[2] B.-T. Chu, On the energy transfer to small disturbances in fluid flow (Part I), Acta Mech. 1 (3) (1965) 215–234. doi:10.1007/BF01387235.

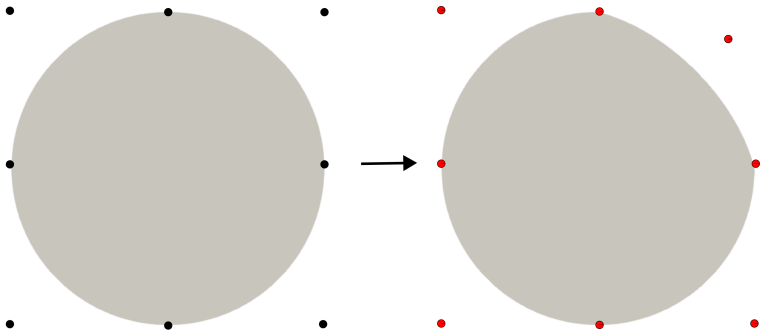

Figure C.17: The unit circle before (left) and after (right) deformation.

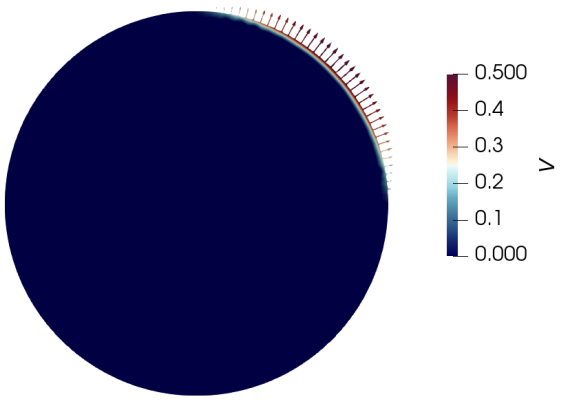

Figure C.18: The displacement field of the 2nd control point. This field is used for the calculation of the shape gradient of the control point in the outward normal direction.

[3] M. P. Juniper, R. Sujith, Sensitivity and Nonlinearity of Thermoacoustic Oscillations, Annu. Rev. Fluid Mech. 50 (1) (2018) 661–689. doi:10.1146/

annurev-fluid-122316-045125.

[4] H. C. Mongia, T. J. Held, G. C. Hsiao, R. P. Pandalai, Challenges and Progress in Controlling Dynamics in Gas Turbine Combustors, J. Propuls. Power 19 (5) (2003) 822–829. doi:10.2514/2.6197.

[5] A. P. Dowling, S. R. Stow, Acoustic Analysis of Gas Turbine Combustors, J. Propuls. Power 19 (5) (2003) 751–764. doi:10.2514/2.6192.

[6] F. Nicoud, L. Benoit, C. Sensiau, T. Poinsot, Acoustic Modes in Combustors with Complex Impedances and Multidimensional Active Flames, AIAA J. 45 (2) (2007) 426–441. doi:10.2514/1.24933.

[7] G. A. Mensah, Efficient computation of thermoacoustic modes, Ph.D. thesis, Technische Universität Berlin (2019).

[8] A. Orchini, C. F. Silva, G. A. Mensah, J. P. Moeck, Thermoacoustic modes of intrinsic and acoustic origin and their interplay with exceptional points, Combustion and Flame 211 (2020) 83–95.

[9] L. Gicquel, G. Staffelbach, T. Poinsot, Large Eddy Simulations of gaseous flames in gas turbine combustion chambers, Prog. Energy Combust. Sci. 38 (6) (2012) 782–817. doi:10.1016/j.pecs.2012.04.004.

[10] E. Motheau, F. Nicoud, T. Poinsot, Mixed acoustic–entropy combustion instabilities in gas turbines, Journal of Fluid Mechanics 749 (2014) 542–576.

[11] L. Magri, M. P. Juniper, Sensitivity analysis of a time-delayed thermo-acoustic system via an adjoint-based approach, J. Fluid Mech. 719 (2013) 183–202. doi:10.1017/jfm.2012.639.

[12] N. P. Jamieson, G. Rigas, M. P. Juniper, Experimental sensitivity analysis via a secondary heat source in an oscillating thermoacoustic system, International Journal of Spray and Combustion Dynamics 9 (4) (2017) 230–240.

[13] J. G. Aguilar, M. P. Juniper, Thermoacoustic stabilization of a longitudinal combustor using adjoint methods, Phys. Rev. Fluids 5 (8) (2020) 083902. doi:10.1103/PhysRevFluids.5.083902.

[14] J. G. Aguilar, M. P. Juniper, Adjoint Methods for Elimination of Thermoacoustic Oscillations in a Model Annular Combustor via Small Geometry Modifications, in: Vol. 4A Combust. Fuels, Emiss., American Society of Mechanical Engineers, 2018, pp. 1–11. doi:10.1115/GT2018-75692.

[15] C. F. Silva, L. Magri, T. Runte, W. Polifke, Uncertainty Quantification of Growth Rates of Thermoacoustic Instability by an Adjoint Helmholtz Solver, J. Eng. Gas Turbines Power 139 (1) (2017) 1–11. doi:10.1115/1.4034203.

[16] G. A. Mensah, J. P. Moeck, Acoustic Damper Placement and Tuning for Annular Combustors: An Adjoint-Based Optimization Study, J. Eng. Gas Turbines Power 139 (6) (2017) 1–9. doi:10.1115/1.4035201.

[17] G. A. Mensah, L. Magri, A. Orchini, J. P. Moeck, Effects of Asymmetry on Thermoacoustic Modes in Annular Combustors: A Higher-Order Perturbation Study, J. Eng. Gas Turbines Power 141 (4) (2019) 041030. doi:10.1115/1.4041007.

[18] G. A. Mensah, A. Orchini, J. P. Moeck, Adjoint-based computation of shape sensitivity in a Rijke-tube, Proc. Int. Congr. Acoust. 2019-Septe (1) (2019) 5489–5496.

[19] S. Falco, M. P. Juniper, Shape optimization of thermoacoustic systems using a 2d adjoint helmholtz solver, in: Turbo Expo: Power for Land, Sea, and Air, Vol. 84126, American Society of Mechanical Engineers, 2020, p. V04AT04A051.

[20] M. P. Juniper, Sensitivity analysis of thermoacoustic instability with adjoint Helmholtz solvers, Phys. Rev. Fluids 3 (11) (2018) 110509. doi:10.1103/PhysRevFluids.3.110509.

[21] L. Magri, Adjoint Methods as Design Tools in Thermoacoustics, Appl. Mech. Rev. 71 (2). doi:10.1115/1.4042821.

[22] S. Xu, W. Jahn, J.-D. Müller, Cad-based shape optimisation with cfd using a discrete adjoint, International Journal for Numerical Methods in Fluids 74 (3) (2014) 153–168.

[23] D. Srinath, S. Mittal, An adjoint method for shape optimization in unsteady viscous flows, Journal of Computational Physics 229 (6) (2010) 1994–2008.

[24] M. Pini, G. Persico, D. Pasquale, S. Rebay, Adjoint method for shape optimization in real-gas flow applications, Journal of Engineering for Gas Turbines and Power 137 (3) (2015) 032604.

[25] C. Sensiau, F. Nicoud, T. Poinsot, A Tool to Study Azimuthal Standing and Spinning Modes in Annular Combustors, Int. J. Aeroacoustics 8 (1) (2009) 57–67. doi:10.1260/147547209786235037.

[26] S. Rienstra, A. Hirschberg, An Introduction to Acoustics, Eindhoven University of Technology, 2004.

[27] M. S. Alnæs, J. Blechta, J. Hake, A. Johansson, B. Kehlet, A. Logg, C. Richardson, J. Ring, M. E. Rognes, G. N. Wells, The fenics project version 1.5, Archive of Numerical Software 3 (100). doi:10.11588/ans.2015.100.20553.

[28] A. Logg, K.-A. Mardal, G. N. Wells, et al., Automated Solution of Differential Equations by the Finite Element Method, Springer, 2012. doi:10.1007/978-3-642-23099-8.

[29] M. S. Alnæs, A. Logg, K. B. Ølgaard, M. E. Rognes, G. N. Wells, Unified form language: A domain-specific language for weak formulations of partial differential equations, ACM Transactions on Mathematical Software (TOMS) 40 (2) (2014) 1–37.

[30] V. Hernandez, J. E. Roman, V. Vidal, SLEPC: A scalable and flexible toolkit for the solution of eigenvalue problems, ACM Trans. Math. Softw. 31 (3) (2005) 351–362. doi:10.1145/1089014.1089019.

[31] S. Balay, S. Abhyankar, M. Adams, J. Brown, P. Brune, K. Buschelman, L. Dalcin, A. Dener, V. Eijkhout, W. Gropp, et al., Petsc users manual.

[32] W. Gropp, E. Lusk, N. Doss, A. Skjellum, A high-performance, portable implementation of the mpi message passing interface standard, Parallel computing 22 (6) (1996) 789–828.

[33] J. Brewster, M. P. Juniper, Shape sensitivity of eigenvalues in hydrodynamic stability, with physical interpretation for the flow around a cylinder, Eur. J. Mech. - B/Fluids 80 (2020) 80–91. doi:10.1016/j.euromechflu.2019.11.007.

[34] P. Grinfield, Introduction to tensor analysis and the calculus of moving surfaces, Springer, 2013.

[35] S. Schmidt, V. Schulz, Shape derivatives for general objective functions and the incompressible Navier-Stokes equations, Control Cybern. 39 (3) (2010) 677–713.

[36] D. A. Ham, L. Mitchell, A. Paganini, F. Wechsung, Automated shape differentiation in the unified form language, Structural and multidisciplinary optimization 60 (2019) 1813–1820.

[37] J. Sokolowski, J.-P. Zolesio, Introduction to Shape Optimization, Vol. 16 of Springer Series in Computational Mathematics, Springer Berlin Heidelberg, Berlin, Heidelberg, 1992. arXiv:arXiv:1011.1669v3, doi:10.1007/978-3-642-58106-9.

[38] M. C. Delfour, J. P. Zolésio, Shapes and Geometries, 2nd Edition, Society for Industrial and Applied Mathematics, 2011. doi:10.1137/1.9780898719826.

[39] M. Sonntag, S. Schmidt, N. R. Gauger, Shape derivatives for the compressible Navier-Stokes equations in variational form, J. Comput. Appl. Math. 296 (2016) 334–351. arXiv:1312.5861, doi:10.1016/j.cam.2015.09.010.

[40] D. Durox, J. F. Bourgouin, M. Philip, T. Schuller, S. Candel, Nonlinear interactions in combustion instabilities coupled by azimuthal acoustic modes, in: Int. Summer Sch. Work. Non-Normal Nonlinear Eff. Aero- Thermoacoustics, Munich, 2013, pp. 1–14.

[41] J.-F. Bourgouin, D. Durox, J. P. Moeck, T. Schuller, S. Candel, Characterization and Modeling of a Spinning Thermoacoustic Instability in an Annular Combustor Equipped With Multiple Matrix Injectors, J. Eng. Gas Turbines Power 137 (2) (2015) 1–11. doi:10.1115/1.4028257.

[42] J. Bourgouin, D. Durox, J. Moeck, T. Schuller, S. Candel, A new pattern of instability observed in an annular combustor: The slanted mode, Proc. Combust. Inst. 35 (3) (2015) 3237–3244. doi:10.1016/j.proci.2014.06.029.

[43] D. Laera, T. Schuller, K. Prieur, D. Durox, S. M. Camporeale, S. Candel, Flame Describing Function analysis of spinning and standing modes in an annular combustor and comparison with experiments, Combust. Flame 184 (2017) 136–152. doi:10.1016/j.combustflame.2017.05.021.

[44] L. Piegl, W. Tiller, The NURBS book, Springer Science & Business Media, 1996.

[45] C. Geuzaine, J.-F. Remacle, Gmsh: A 3-d finite element mesh generator with built-in pre-and post-processing facilities, International journal for numerical methods in engineering 79 (11) (2009) 1309–1331.

[46] B. Gustavsen, A. Semlyen, Rational approximation of frequency domain responses by vector fitting, IEEE Trans. Power Deliv. 14 (3) (1999) 1052–1061. doi:10.1109/61.772353.

[47] B. Gustavsen, Improving the Pole Relocating Properties of Vector Fitting, IEEE Trans. Power Deliv. 21 (3) (2006) 1587–1592. doi:10.1109/TPWRD.2005.860281.

[48] G. A. Mensah, L. Magri, A. Orchini, J. P. Moeck, Effects of asymmetry on thermoacoustic modes in annular combustors: a higher-order perturbation study, Journal of Engineering for Gas Turbines and Power 141 (4) (2019) 041030.

[49] O. Tammisola, M. P. Juniper, Coherent structures in a swirl injector at Re = 4800 by nonlinear simulations and linear global modes, J. Fluid Mech. 792 (2016) 620–657. doi:10.1017/jfm.2016.86.

[50] T. L. Kaiser, G. Varillon, W. Polifke, F. Zhang, T. Zirwes, H. Bockhorn, K. Oberleithner, Modelling the response of a turbulent jet flame to acoustic forcing in a linearized framework using an active flame approach, Combustion and Flame 253 (2023) 112778.

[51] T. Poinsot, D. Veynante, Theoretical and numerical combustion, RT Edwards, Inc., 2005.